

## BASIC PARAMETER ESTIMATION OF BINARY NEUTRON STAR SYSTEMS BY THE ADVANCED LIGO/VIRGO NETWORK

CARL L. RODRIGUEZ<sup>1</sup> BENJAMIN FARR<sup>1</sup> VIVIEN RAYMOND<sup>1,2</sup> WILL M. FARR<sup>1</sup> TYSON LITTENBERG<sup>1</sup> DIEGO FAZI<sup>1</sup> VICKY KALOGERA<sup>1</sup>

*Draft version September 3, 2013*

### ABSTRACT

Within the next five years, it is expected that the Advanced LIGO/Virgo network will have reached a sensitivity sufficient to enable the routine detection of gravitational waves. Beyond the initial detection, the scientific promise of these instruments relies on the effectiveness of our physical parameter estimation capabilities. The majority of this effort has been towards the detection and characterization of gravitational waves from compact binary coalescence, e.g. the coalescence of binary neutron stars. While several previous studies have investigated the accuracy of parameter estimation with advanced detectors, the majority have relied on approximation techniques such as the Fisher Matrix. Here we report the statistical uncertainties that will be achievable for optimal detection candidates ( $\text{SNR} = 20$ ) using the full parameter estimation machinery developed by the LIGO/Virgo Collaboration via Markov-Chain Monte Carlo methods. We find the recovery of the individual masses to be fractionally within 9% (15%) at the 68% (95%) credible intervals for equal-mass systems, and within 1.9% (3.7%) for unequal-mass systems. We also find that the Advanced LIGO/Virgo network will constrain the locations of binary neutron star mergers to a median uncertainty of 5.1 deg<sup>2</sup> (13.5 deg<sup>2</sup>) on the sky. This region is improved to 2.3 deg<sup>2</sup> (6 deg<sup>2</sup>) with the addition of the proposed LIGO India detector to the network. We also report the average uncertainties on the luminosity distances and orbital inclinations of ideal detection candidates that can be achieved by different network configurations.

### 1. INTRODUCTION

Within the next few years, the first generation of gravitational-wave interferometers capable of regularly detecting astrophysical sources will come online (Harry & the LIGO Scientific Collaboration 2010; Virgo Collaboration 2009). The Advanced LIGO and Advanced Virgo detectors (and the anticipated LIGO India detector) will provide the first insights into the final moments of binary compact object mergers, including the mergers of binary neutron star systems. Intense preparations are underway to characterize and extract as much physical information as possible from these signals.

The mergers of binary neutron stars (BNS) are expected to be one of the most common compact binary sources in the advanced detector era. Models from stellar evolution and observations of binary pulsars suggest that the number of BNS mergers within Advanced LIGO/Virgo's detection horizon could reach several tens to hundreds each year (Abadie et al. 2010). Although the peak sensitivity of ground-based detectors is not focused on the frequency at which BNS systems merge, it could still be possible to extract information about both strong field gravitational physics (Li et al. 2012) and the equation of state of dense nuclear matter (Hinderer et al. 2010). Furthermore, the observations of multiple BNS systems will provide key insights into the evolution of binary systems in the field (Kalogera et al. 2004; Kim

et al. 2006; Oslowski et al. 2011; O'Shaughnessy et al. 2010). As such, BNS systems will likely form the “bread and butter” of the compact binary coalescence detection effort in the coming years.

Of course one must distinguish between the detection of such events and the precision measurement of their relevant physical parameters. The detection of BNS systems will be performed with a matched filtering approach. By comparing the data stream with a bank of theoretical templates, the time-series data can be searched for candidate signals at a sufficiently rapid rate to analyze months of data. See Abadie et al. (2012). However, the parameter space of these signals can be highly degenerate, with several locations in parameter space corresponding to waveforms with nearly identical overlap. In order to fully realize the science potential of these instruments, we must perform a full exploration of the parameter space for each detection. By analyzing the parameter space of each candidate with a Bayesian inference technique, we will be able to make informative, scientifically meaningful statements about the physics of these systems. To that end, we employ a Markov-Chain Monte Carlo sampling algorithm, `lalinference_mcmc`, included in the LIGO Algorithm Library parameter estimation code, `LALInference`, to analyze the parameter space of BNS systems.

By employing the full parameter-estimation machinery that will eventually be used in the Advanced LIGO/Virgo era, our results give realistic estimates of the capabilities of advanced ground-based detectors to characterize BNS systems. Until recently, the majority of studies have employed the Fisher-matrix formalism which was first adapted for gravitational-wave parame-

<sup>1</sup> Center for Interdisciplinary Exploration and Research in Astrophysics (CIERA) & Dept. of Physics and Astronomy, Northwestern University, 2145 Sheridan Rd, Evanston, IL 60208, USA; [e-mail: [cr@u.northwestern.edu](mailto:cr@u.northwestern.edu)]

<sup>2</sup> California Institute of Technology, Pasadena, CA 91125, USA

ter estimation by Finn (1992). While each of these studies (Poisson & Will 1995; Cutler & Flanagan 1994; Arun et al. 2005) have pointed out the limitations and flaws of the Fisher Information Matrix, there has been relatively few studies which investigate the BNS parameter estimation capabilities of Advanced LIGO/Virgo using the techniques that will eventually be employed. The recent work of Vallisneri (2008) and our own work (Rodriguez et al. 2013) has demonstrated that the Fisher matrix cannot even be treated as a lower bound on the standard deviations of certain parameters (particularly the masses) measurable in gravitational-wave detectors. While previous studies have employed MCMC techniques for specific parameters, (Nissanke et al. 2011, 2013; Veitch et al. 2012), none have considered the full range of parameters, in particular the neutron star masses.

In this paper, we perform a systematic study of the statistical uncertainties with which the Advanced LIGO/Virgo network will be able to measure the basic parameters of BNS mergers. In Section 2, we describe the machinery of our parameter estimation code, `LALInference`, and the associated MCMC sampler, `lalinference_mcmc`, as well as the frequency-domain gravitational-wave template we employ. In Section 3, we qualitatively analyze the posterior probability density functions for BNS systems with different masses and extrinsic parameters. We select three equal-mass and one unequal-mass binary systems as prototypical examples of BNS systems. Each system is analyzed 40 times with isotropically selected sky locations and orbital orientations, and with a distance such that each signal was injected with a network signal-to-noise ratio of 20. The results are divided into three subsections of interest: the recovery of the mass parameters (Section 3.1), the recovery of the orbital inclination and luminosity distance (Section 3.2), and the localization of sources on the sky (Section 3.3). Finally we provide quantitative 1-dimensional credible intervals on each parameter in Section 4. These results, contained in Tables 1 and 2, are intended as a reference for the optimal BNS parameter estimation capabilities of Advanced LIGO/Virgo. We assume that  $G = c = 1$  throughout.

## 2. PARAMETER ESTIMATION

We begin by introducing a Bayesian formalism for parameter estimation. We assume that the time-domain signal in a gravitational-wave network can be written as the sum of a gravitational waveform  $h_0$  and the noise of the detector  $n$ . We further assume that this noise is stationary and Gaussian with zero mean. The detector output is simply

$$s = n + h_0. \quad (1)$$

Since the noise model is Gaussian, we can write the probability of a specific signal realization  $s$  given an input waveform  $h(\boldsymbol{\theta})$  as proportional to the probability that the residual is Gaussian distributed once the waveform has been subtracted

$$\begin{aligned} p(s|\boldsymbol{\theta}) &\propto \exp\left[-\frac{1}{2}\langle n|n\rangle\right] \\ &= \exp\left[-\frac{1}{2}\langle s - h(\boldsymbol{\theta})|s - h(\boldsymbol{\theta})\rangle\right], \end{aligned} \quad (2)$$

where  $\boldsymbol{\theta}$  is the set of parameters for the template waveforms. The quantity  $p(s|\boldsymbol{\theta})$  is the likelihood of the signal  $s$  given the parameters  $\boldsymbol{\theta}$ . The inner product,  $\langle \cdot | \cdot \rangle$ , is defined using the noise spectrum of the detectors as

$$\langle a|b \rangle \equiv 4\Re \int \frac{\tilde{a}(f)\tilde{b}^*(f)}{S_n(f)} df, \quad (3)$$

where  $S_n(f)$  is the one-sided power-spectral density (PSD) as a function of frequency, and  $\tilde{a}(f)$  and  $\tilde{b}(f)$  are the Fourier transforms of the time-domain data  $a(t)$  and  $b(t)$ . If we pick a set of parameters  $\boldsymbol{\theta}$  such that  $h(\boldsymbol{\theta}) = h_0$ , then the likelihood (2) will be near a global maximum; however, the presence of noise will in general deflect the maximum of our likelihood away from the value at  $h(\boldsymbol{\theta}) = h_0$ . Therefore, the maximum likelihood parameters do not necessarily correspond to the true parameters of the source.

Once we have the likelihood of the signal (2), we employ Bayes Theorem to obtain the posterior probability of the system parameters  $\boldsymbol{\theta}$  given the signal  $s$  as

$$\begin{aligned} p(\boldsymbol{\theta}|s) &= \frac{p(\boldsymbol{\theta})p(s|\boldsymbol{\theta})}{p(s)} \\ &\propto p(\boldsymbol{\theta}) \exp\left[-\frac{1}{2}\langle s - h(\boldsymbol{\theta})|s - h(\boldsymbol{\theta})\rangle\right], \end{aligned} \quad (4)$$

where  $p(\boldsymbol{\theta})$  are the prior probabilities on our source parameters and  $p(s)$  is a normalization constant.

We are interested in the posterior  $p(\boldsymbol{\theta}|s)$  as it encodes information about the prior state of knowledge about the problem in addition to the likelihood of the signal. For instance, since it is assumed that compact binaries form homogeneously in the local universe observable by advanced detectors, we can safely assume that the population of sources will be distributed homogeneously in volume, i.e. with a density proportional to the square of the luminosity distance  $D^2$ . Our prior information can come from mathematical limits in the parameter space or from our *a priori* knowledge of astrophysical systems. We employ priors which are

- uniform in component masses from  $0.8M_{\odot} \leq M_{1,2} \leq 30M_{\odot}$ , with a minimum chirp mass (see Eq. (7)) of  $0.6M_{\odot}$ ,
- uniform in volume, which implies a luminosity distance prior of  $p(D)dD \propto D^2dD$ ,
- uniform in coalescence time over the segment of data being analyzed,
- a delta function at zero spin, and
- isotropic in all angles

The mass priors listed here are the generic priors used in follow-up analysis, not specifically for BNS systems. While we could have used a prior with a lower component mass cutoff for the present study, in practice the higher prior boundary does not affect our current analysis.

### 2.1. Markov-Chain Monte Carlo

The LIGO Algorithm Library Bayesian inference code, `LALInference`, is designed as a unified framework for

gravitational-wave parameter estimation. By using a common setup for waveform generation, PSD estimation, data handling, and other associated techniques from gravitational-wave parameter estimation, `LALInference` allows the implementation of multiple samplers of the parameter space, including Nested Sampling (`lalinference_nest`, described in Veitch & Vecchio (2010)) and Markov-Chain Monte Carlo (`lalinference_mcmc`). We elect to use the MCMC sampler for this study. `lalinference_mcmc` is based upon the previously described code, `SpinSpiral` (van der Sluys et al. 2009; Raymond et al. 2010). The MCMC employs a Metropolis-Hastings sampling algorithm, which can be described as follows (Gilks 1999):

1. Pick an initial point in the parameter space ( $\boldsymbol{\theta}_{\text{old}}$ ), and then propose a random “jump” to a new set of waveform parameters,  $\boldsymbol{\theta}_{\text{new}}$ . The jump follows the proposal distribution  $q(\boldsymbol{\theta}_{\text{new}}|\boldsymbol{\theta}_{\text{old}})$ .
2. Calculate the posterior probability,  $p(\boldsymbol{\theta}_{\text{new}}|s)$ , of the new parameters using (2) and (4).
3. Accept the new parameters with probability

$$p_{\text{accept}} = \min \left[ 1, \frac{p(\boldsymbol{\theta}_{\text{new}}|s)q(\boldsymbol{\theta}_{\text{old}}|\boldsymbol{\theta}_{\text{new}})}{p(\boldsymbol{\theta}_{\text{old}}|s)q(\boldsymbol{\theta}_{\text{new}}|\boldsymbol{\theta}_{\text{old}})} \right]. \quad (5)$$

If the new parameters are accepted, record  $\boldsymbol{\theta}_{\text{new}}$  and repeat with  $\boldsymbol{\theta}_{\text{new}} \rightarrow \boldsymbol{\theta}_{\text{old}}$ ; otherwise, record  $\boldsymbol{\theta}_{\text{old}}$ , and repeat.

The above procedure is designed to record a chain of samples whose distribution is  $p(\boldsymbol{\theta}|s)$ . By drawing a sufficient ( $\sim 1000$ ) number of effectively independent samples from the posterior, the chains traces out the functional form of the posterior, gathering more samples from regions with high posterior probability density. Depending on the proposal distribution,  $q$ , the convergence (mixing) of the chain may be rapid or slow. We employ multiple optimization techniques, including both specially-crafted jump proposals ( $q$ ) and parallel tempering, to ensure adequate mixing of the Markov Chains throughout our parameter space. Both samplers were tuned and developed during the last science run of the Initial LIGO/Virgo network. A description of the parameter estimation capabilities of these two samplers with respect to real interferometer data, as well as a more detailed description of the algorithms and checks for convergence, can be found in the LIGO Scientific Collaboration et al. (2013).

## 2.2. Waveform Model

We use a frequency-domain waveform accurate up to 3.5 post-Newtonian (pN) order in phase and 3 pN order in amplitude of the lowest ( $l = m = 2$ ) spatial mode. We restrict ourselves to quasi-circular, non-spinning waveforms as a simplifying assumption. The standard form of our waveform model, known as the *TaylorF2* approximant, is calculated via the stationary-phase approximation. In this setup, the gravitational-wave amplitude is given by

$$\tilde{h}(f) = a(t_f)e^{i\psi(f)}, \quad (6)$$

where  $a(t_f)$  is the amplitude evaluated at a stationary-phase reference point, which to lowest order takes the

form  $a(t_f) \propto f^{-7/6} \mathcal{M}_c^{5/6} \Theta(\text{angle})/D$ , where  $D$  is the luminosity distance of the binary, and  $\psi(f)$  is the pN phase.  $\Theta(\text{angle})$  is a function of the orbital orientation with respect to the detector network in terms of the sky position, orbital inclination, and the wave polarization. In addition to the total mass,  $M_{\text{tot}} \equiv M_1 + M_2$ , it is convenient to work with the mass ratio and chirp mass, defined by

$$q \equiv M_2/M_1 \quad \text{and} \quad \mathcal{M}_c = (M_1 M_2)^{3/5} M_{\text{tot}}^{-1/5}, \quad (7)$$

respectively.<sup>3</sup> By convention,  $M_1 \geq M_2$ . The stationary phase then becomes an expansion in the Newtonian orbital velocity,  $v = (\pi M_{\text{tot}} f)^{1/3}$ ,

$$\psi(f) = 2\pi f t_c - \phi_0 + \frac{\pi}{4} + \frac{3}{128} \left( \frac{M_{\text{tot}}}{\mathcal{M}_c} \right)^{5/3} \sum_{k=0}^n \alpha_k v^{k-5} \quad (8)$$

where the  $\alpha_k$  coefficients are taken from the pN expansion to order  $n/2$ . See Buonanno et al. (2009) for a description and comparison of different waveform families. The terms  $t_c$  and  $\phi_0$  in equation (8) are constants of integration, referred to as the chirp time and coalescence phase, respectively.

We consider the mass parameters ( $\mathcal{M}_c, q$ ) and the phasing parameters,  $(\phi_0, t_c)$ , to be the intrinsic parameters of the gravitational-wave signal. There are an additional 5 extrinsic parameters, independent of the pN orbital phase, which can modulate the amplitude of the signal independently in each detector. Combining these leads to our 9-dimensional parameter space for non-spinning systems,

$$\boldsymbol{\theta} = (\mathcal{M}_c, q, \phi_0, t_c, D, \iota, \psi, \alpha, \delta), \quad (9)$$

where

- $\mathcal{M}_c$  is the chirp mass,
- $q$  is the mass ratio,
- $\phi_0$  and  $t_c$  are the chirp phase and chirp time, arbitrary phasing parameters,
- $D$  is the luminosity distance to the binary,
- $\iota$  is the orbital inclination (the angle between the orbital angular momentum and the line of sight),
- $\psi$  is the gravitational-wave polarization, and
- $\alpha$  and  $\delta$  are the right ascension and declination of the source on the sky.

Since the wave amplitude depends on the orientation of the binary with respect to each detector, most of the information about these extrinsic parameters comes from two sources: the time-of-arrival triangulation of the signal, and the relative amplitudes in each detector in the network.

<sup>3</sup> Most gravitational-wave literature instead uses the *symmetric mass ratio*, defined as  $\eta \equiv M_1 M_2 / M^2$ . We elect to use  $q$  as it is more physically intuitive, and because it avoids an integrable singularity that can appear for equal-mass systems when employing a prior on  $p(\eta)$ .

### 2.3. Detector Configuration and Noise Models

To perform the integral defined in (3), we used as our power-spectral density the best estimate for a high-power, zero-detuning configuration of Advanced LIGO, provided by the LIGO Scientific Collaboration. Both the noise curve and technical reports describing it can be found in Shoemaker (2009). We consider two configurations of the advanced detector network: a three-detector configuration consisting of the two LIGO sites (in Hanford, WA and Livingston, LA) and the Virgo site (in Pisa, Italy), and a four-detector configuration that adds the proposed LIGO-India detector (in Chitradurga, KA). For simplicity, we assume each detector to be operating at the Advanced LIGO sensitivity.

For a multi-detector network, the noise-weighted inner products (3) combine linearly, allowing us to use the above formalism with minimal modification. We integrate the inner product from a lower-frequency cutoff of 20Hz to the innermost-stable-circular orbit of the systems, which for a non-spinning binary is a function only of the total mass:

$$\pi f_{\text{ISCO}} = \frac{1}{6^{3/2} M_{\text{tot}}} \cdot \quad (10)$$

We define the signal-to-noise ratio (SNR) of a gravitational wave in a single detector as

$$\rho \equiv \frac{4}{\sigma} \int_0^\infty \frac{|\tilde{s}(f)\tilde{h}(f)|}{S_n(f)} df, \quad (11)$$

where  $\rho$  is the SNR and  $\tilde{s}(f)$  and  $\tilde{h}^*(f)$  are the frequency-domain data and template, respectively, and the normalization  $\sigma$  is given by

$$\sigma^2 = 4 \int_0^\infty \frac{|\tilde{h}(f)|^2}{S_n(f)} df. \quad (12)$$

When dealing with a network of gravitational-wave detectors, the SNRs of the individual detectors add in quadrature. That is, the network SNR for a detection is

$$\rho_{\text{network}} = \sqrt{\sum_i \rho_i^2} \quad (13)$$

where  $\rho_i$  is the SNR, given by (11), of the  $i^{\text{th}}$  detector.

For this study, we consider four separate populations of BNS systems, with component mass combinations of  $1M_\odot/1M_\odot$ ,  $1.4M_\odot/1.4M_\odot$ ,  $1M_\odot/2.5M_\odot$ , and  $2.5M_\odot/2.5M_\odot$ . Each population consisted of 40 signals distributed randomly in sky location, polarization, inclination, time-of-arrival, and coalescence phase. The luminosity distance,  $D$ , was selected to provide a network SNR of  $\rho_{\text{network}} = 20$  for each source in each network configuration. While unphysical from an astrophysics perspective (binary sources are expected to be distributed uniformly in co-moving volume), this choice allows us to explore the parameter estimation in the context of loud but plausible detection candidates.

Finally, note that the PSD that defines the inner product (3) is simply the time-averaged sensitivity of a given detector to a specific frequency. Ignoring non-Gaussian glitches, any stretch of data should contain

a specific noise realization drawn from a Gaussian colored by the PSD. Without a realistic model including the actual instrument sensitivity, non-stationary noise, and uncertainty in the PSD we cannot accurately simulate gravitational-wave data to the point of making precise predictions about parameter estimation capabilities. Furthermore, the posterior distribution from a future detection will be influenced by the realization of the noise at the time of the detection. Because of this, we elect to focus only on the statistical errors due to the flexibility of the waveforms and the expected sensitivity of the advanced era detectors and suppress any effects of detector noise by picking  $n(t) \equiv 0$ . It can be shown that this “zero-noise” injection represents the geometric mean of the same experiment over many different noise realizations drawn from the same PSD. See Nissanke et al. (2010), c.f. equation 53.

Consequently, what we recover with the MCMC could be interpreted as the posterior distribution function for each source averaged over all possible (Gaussian) noise realizations, assuming we have the correct PSD and that the signal is sufficiently powerful for the linearized-signal approximation (Vallisneri 2008) to be valid. By selecting a source population with an artificial distribution in SNR, we ensure that the “zero-noise” as average uncertainty

To check that our reported statistical errors are not in gross disagreement with those obtained in the presence of noise, we selected a particular simulated signal to perform parameter estimation in several noise realizations. The comparison of the noise-dependent and noise-free results can be found in Section 3.4.

## 3. RESULTS

Of the nine parameters in the domain of the waveform, only six are particularly physically interesting: the masses of the two binaries,  $M_1$  and  $M_2$ , the orbital inclination,  $\iota$ , the angular position on the sky,  $\alpha$  and  $\delta$ , and the luminosity distance of the source,  $D$ . While the coalescence phase  $\phi_0$ , the coalescence time  $t_c$ , and the wave polarization  $\psi$  must be included in any parameter estimation of the waveform, they do not encode any information of particular astrophysical interest.

In Figure 1, we provide an example of the nine, 1-dimensional marginalized posterior probability density functions recovered from a single  $1.4M_\odot/1.4M_\odot$  BNS system. These PDFs are representative of the type of results that will be produced by parameter estimation studies in the advanced detector era. Notice that the peak of several parameters, including the chirp mass,  $\mathcal{M}_c$ , appears to be displaced from the true values in dashed red. This effect is due to the reduction of the 9-dimensional PDF to a series of marginalized 1-dimensional PDFs. For instance, the 1-dimensional PDF for chirp mass is marginalized via

$$p(\mathcal{M}_c|s) = \int_{\boldsymbol{\theta} \setminus \mathcal{M}_c} p(\boldsymbol{\theta}|s) d(\boldsymbol{\theta} \setminus \mathcal{M}_c) \quad (14)$$

where the notation  $\boldsymbol{\theta} \setminus \mathcal{M}_c$  implies all parameter of (9) except  $\mathcal{M}_c$ . Other parameter and higher-dimensional marginalizations follow a similar convention. In practice, the MCMC samples make this integral trivial: since the samples are distributed according to the posterior,

## Example 1D Posterior Probability Densities for $1.4M_{\odot}/1.4M_{\odot}$ System

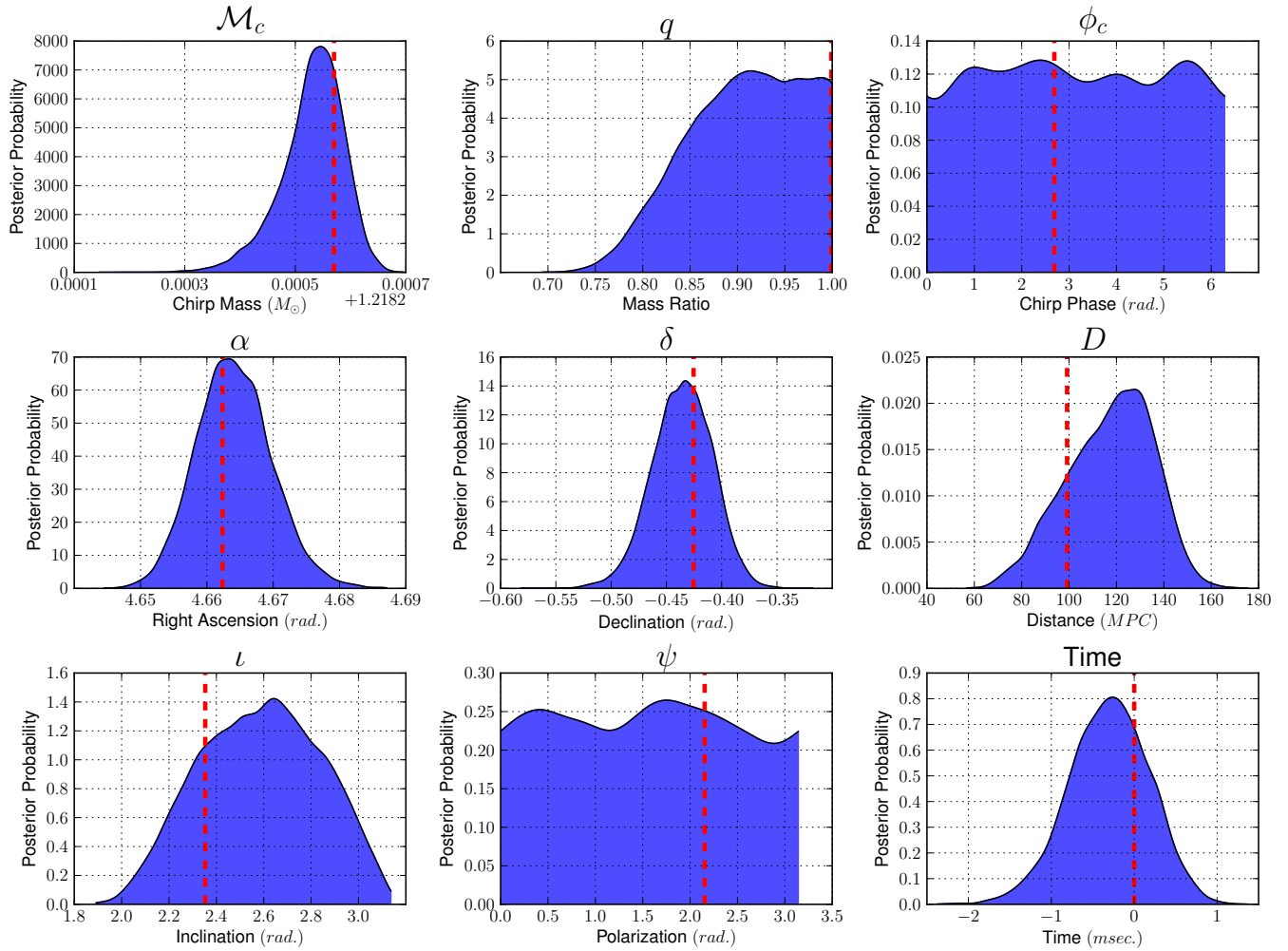


FIG. 1.— Marginalized 1D posterior probability densities of a typical  $1.4M_{\odot}/1.4M_{\odot}$  BNS system. We have plotted each of the 9 parameters for our non-spinning BNS problem as stated in section 2.2. Note how, even for parameters with excellent recovery, the peak of the 1D Gaussian is displaced from the injected value (in dashed red). This is not due to a systematic bias, but is caused by the marginalization of a single dimension from the full 9D posterior space. To better see this effect, compare the 1D PDF for  $\mathcal{M}_c$  and  $q$  with the 2D marginalized PDF in Figure 2. The plots here represent the Gaussian kernel density estimator of each PDF. The estimate for  $q$  was computed by reflecting the highest 10% of samples across the  $q = 1$  boundary. This was done to avoid a false decrease in estimated probability density near the boundary.

(14) can be calculated by simply reading off the relevant samples in a single parameter, implicitly calculating a Monte-Carlo integral over all other parameters.

### 3.1. Mass Parameters

Of the nine variables in our parameter space (9), the mass parameters,  $\mathcal{M}_c$  and  $q$ , or, correspondingly,  $M_1$  and  $M_2$  are the most astrophysically interesting. The ability of Advanced LIGO/Virgo to construct a population of BNS masses will be one of the more useful and immediate applications of gravitational-wave astronomy.

We find that there is virtually no difference between the mass PDFs of our different injected signals within each mass bin. While this may initially seem disconcerting, it is to be expected for the analysis presented here. Recall that all of the BNS signals were injected with a network SNR of 20 into a zero-noise detector realization.

Furthermore, note that the mass parameters are the only two which directly affect the phase of the TaylorF2 waveform (8). Therefore, as long as the injected mass parameters are identical within each mass system, and as long as the injected SNR is identical, the amount of recoverable information in each mass parameter should be almost identical, and for a sufficiently converged MCMC chain, the recovered posterior PDF should be identical.

This effect can be summarized as follows: for non-spinning systems, the posterior probability of the masses,  $p(\mathcal{M}_c, q | s)$ , does not depend strongly on the recovery of the extrinsic parameters,  $\phi_0$  or  $t_c$ . Therefore, systems with identical masses will produce identical mass PDFs. The only noticeable difference will come from the specific realization of noise produced by the detector, which we address in Section 3.4.

In Figures 2 and 3, we show the marginalized 2D poste-

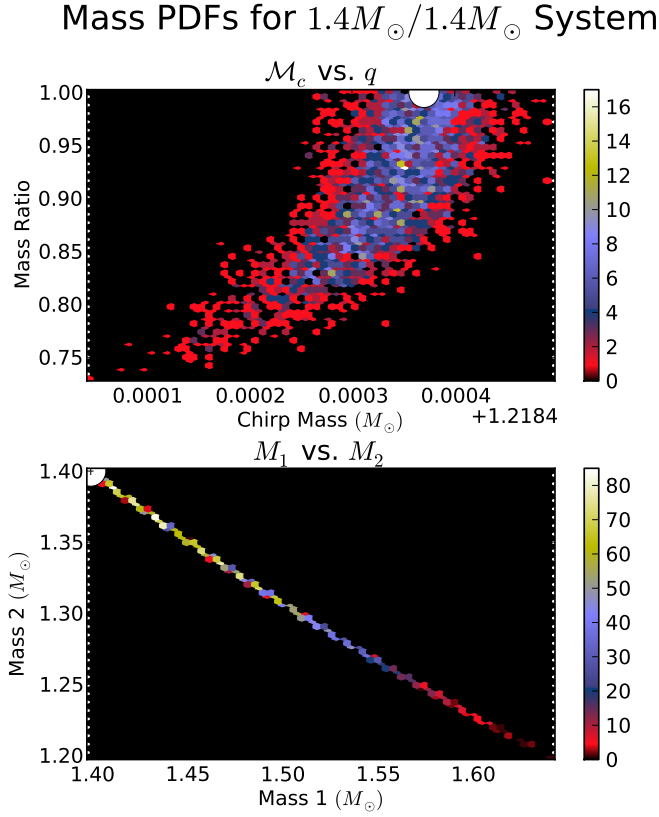


FIG. 2.— 2D marginalized posterior probability density functions for the mass parameters recovered in typical a  $1.4M_{\odot}/1.4M_{\odot}$  system. The posteriors are plotted in terms of parameters used in the waveform, chirp mass ( $\mathcal{M}_C$ ) and the mass ratio ( $q$ ), and in the individual component masses of the binary ( $M_1$  and  $M_2$ ). In the  $\mathcal{M}_c$ - $q$  space, the posterior would almost resemble a Gaussian if not for the limitation of  $q \leq 1$ . The presence of the  $q$  cutoff and the convention that  $M_1 \geq M_2$  inform the non-Gaussian features present. When projected as 1D marginalized posteriors, the component masses resemble the posterior PDFs shown in Figure 4.

prior PDFs of our mass parameters for prototypical equal-mass and unequal-mass binaries. We include the PDF in both the  $\mathcal{M}_c$ - $q$  space (relevant for the waveform and the MCMC algorithm), and the more physically interesting component mass space ( $M_1$ - $M_2$ ). Although only the  $1.4M_{\odot}/1.4M_{\odot}$  system is included in Figure 2, the PDF is qualitatively identical to the other equal mass cases, modulo a scaling factor.

To condense the results into a single figure of merit, we average the 1-dimensional mass PDFs into a single posterior probability for the system in Figure 4. Notice how, when averaged and normalized to the injected values, the recovery of the component masses depends only on the mass ratio. Furthermore, for systems with equal component masses, the posterior barely extends beyond 15% of the injected values. If one assumes that the threshold between black holes and neutron stars lies at approximately  $3M_{\odot}$ , then it might be naively assumed that the mass recovery would allow one to discriminate between black holes and neutron stars.

In practice, there is a physical complication to this claim: we have neglected the spin of the binaries, which will be highly correlated to the masses. This coupling means that, in the case where the black hole spins are

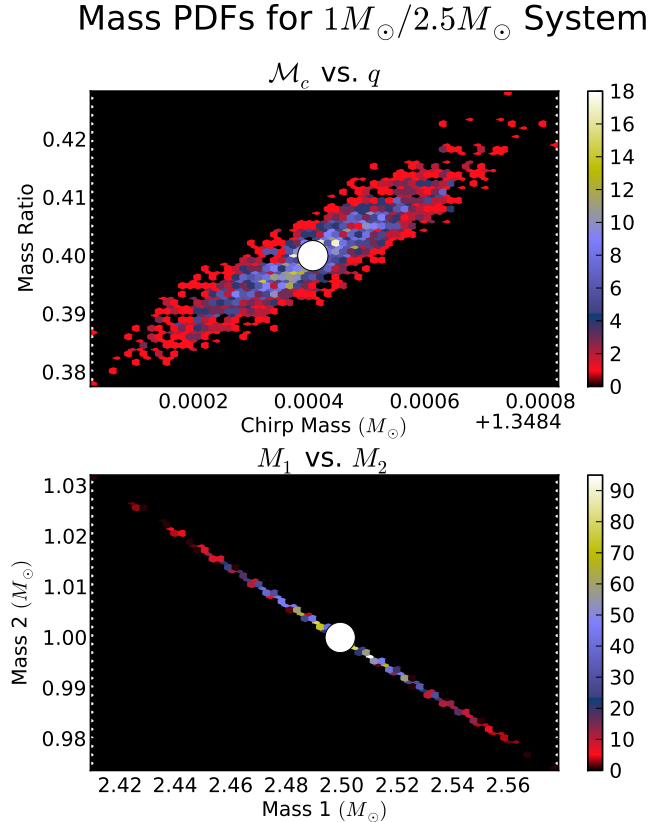


FIG. 3.— Similar to Figure 2, but for a typical  $1M_{\odot}/2.5M_{\odot}$  system. The unequal mass ratio displaces the posterior PDFs from the  $q \leq 1$  boundary present in the equal-mass case, yielding a Gaussian PDF in both the  $\mathcal{M}_c$ - $q$  and  $M_1$ - $M_2$  spaces.

parallel to the orbital angular momentum, a higher-massed spinning black hole systems can produce waveforms very similar to non-spinning, low-mass systems. This effect makes it extremely difficult to discern between non-spinning neutron stars and spin-aligned, more massive black holes (Baird et al. 2013; Hannam et al. 2013). However, the situation is not hopeless: if the spins are misaligned, the spin vectors will couple to the orientation of the binary (encoded in the three angles  $\phi_0$ ,  $\iota$ , and  $\psi$ ) via relativistic precession. It remains to be seen if using fully spinning waveforms will make it possible for Advanced LIGO/Virgo to discern binary neutron stars from their spinning black hole counterparts.

In Table 1, we list the 68% and 95% credible intervals for the mass parameters. We find that the component masses for equal mass systems can be isolated to between 6.4% and 9% (10.3% and 15%) fractional uncertainty at the 68% (95%) credible interval. This value drops to less than 1.9% (3.7%) for the components of the unequal mass systems. Again, this neglects the effects of spin which can substantially increase these values.

### 3.2. Inclination and Distance

Binary neutron star systems (along with neutron star/black hole systems) are one of the best candidates for progenitors of short-hard gamma-ray bursts (Nakar 2007, and references therein). After merger, the remnant is believed to emit the burst along the axis of orbital angular momentum, making the inclination of the binary

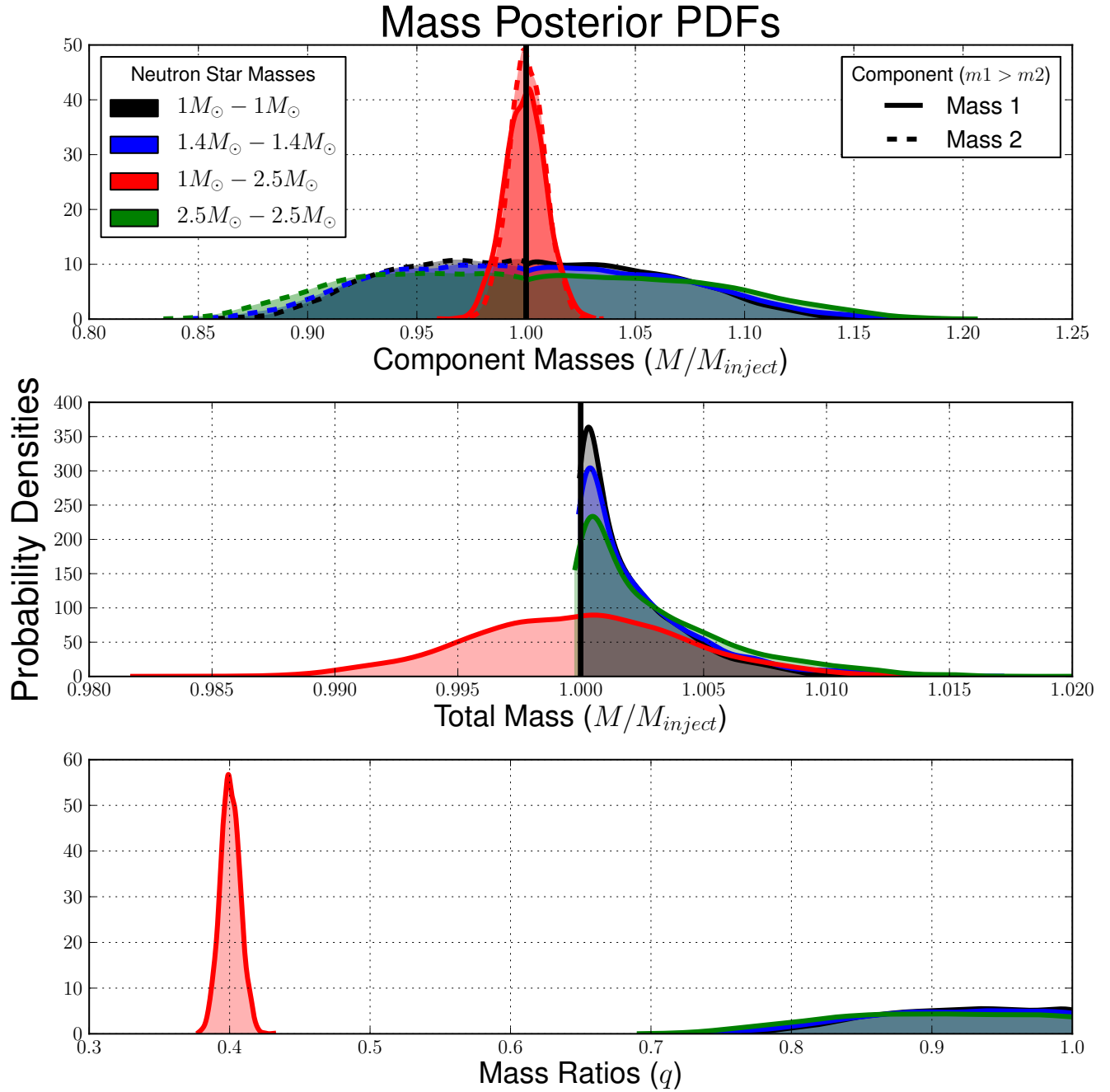


FIG. 4.— Mass PDFs for the four BNS systems, averaged over each of the 40 injections. The average is reported since, in practice, there was quantitatively no difference between the recovered PDFs for different systems with identical masses and SNRs. Systems with identical mass ratios but different total masses have quantitatively identical PDFs when normalized to the total mass. Similarly to Fig. 1, we plot the Gaussian kernel density estimates, and reflect 10% of the points across the  $q = 1$  and  $M_1 = M_2$  boundaries (for the three equal-mass cases).

system of particular interest to gamma-ray astronomy (Abadie et al. 2010; Corsi et al. 2012). The inclination is detected as a relative amplitude difference between the two gravitational-wave polarizations, such that to lowest order:

$$h_+(f) = \frac{1 + \cos^2(\iota)}{2D} \tilde{h}(f)$$

$$h_\times(f) = i \frac{\cos(\iota)}{D} \tilde{h}(f). \quad (15)$$

It should be apparent that the luminosity distance  $D$  and the inclination  $\iota$  can be highly correlated in any parameter estimation recovery.

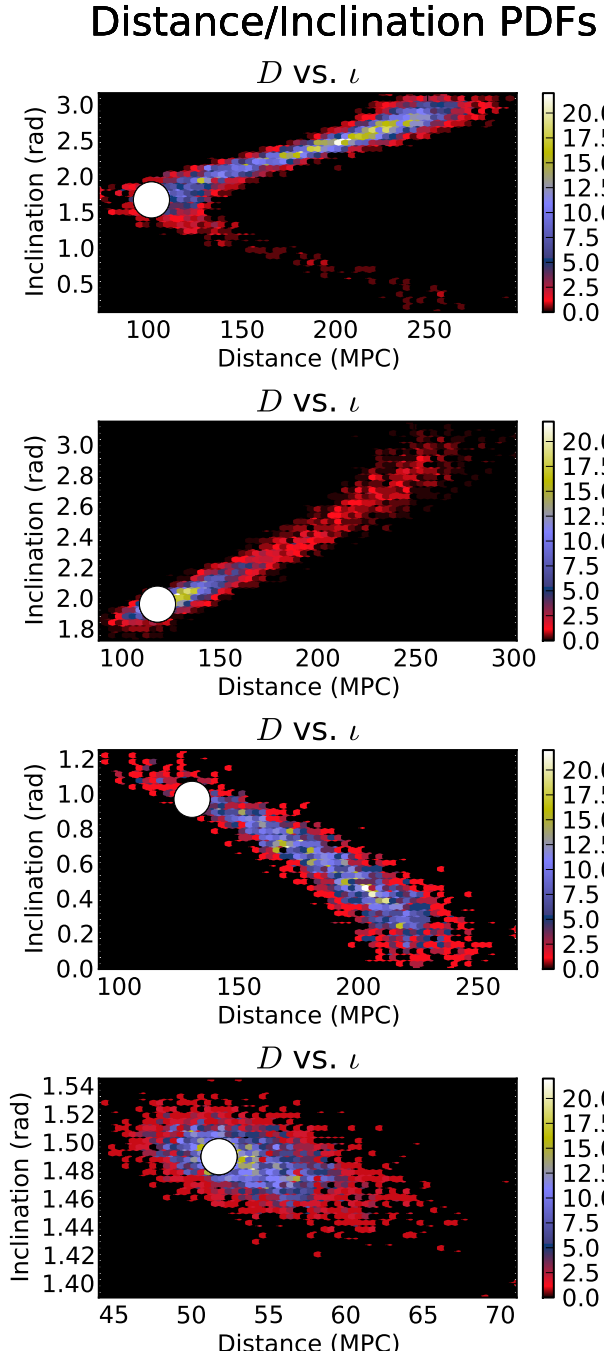


FIG. 5.— Typical marginalized 2D mass PDFs for luminosity distance  $D$  and orbital inclination  $\iota$ . Notice the bimodal distribution on the first PDF, that can occur when a system is detected nearly “edge-on” ( $\iota \approx \pi/2$ ). In general, the degeneracy between distance and inclination forces the PDF into one of these two paths when the system is not edge-on, as seen in the second and third PDFs.

Given this degeneracy, it should come as no surprise that the 2D marginalized posteriors of distance and inclination are the broadest of the six physically interesting parameters. Four typical 2D PDFs are presented in Figure 5. Notice the bimodal uncertainty present in the top 2D PDF along the  $\iota$  axis, due to the similarity between

the evaluated likelihoods at  $\iota$  and  $\iota + \pi/2$ . As the majority of the information extracted via parameter estimation is from the phase of the signal, the recovery of the posterior in  $D\text{-}\iota$  space will be limited, even during the Advanced LIGO/Virgo era; however, if a gravitational-wave signal is matched to a detected SGRB counterpart (which may occur at the rate of  $\sim 3\text{yr}^{-1}$  in Advanced LIGO/Virgo, according to Metzger & Berger (2012)), the optical information about the orbital inclination will provide an additional constraint on the  $D\text{-}\iota$  space, vastly improving the luminosity distance recovery quoted here. These results qualitatively agree with those of Nissanke et al. (2011), who studied in detail MCMC estimation of  $D\text{-}\iota$  measurements from gravitational-wave detectors with coincident GRB detections.

In Table 2, we list the averaged 68% and 95% credible intervals for distance and inclination. Notice that the uncertainties on distance can be extreme, from tens to hundreds of Mpc. When discussing the inclination angle, we elected to use  $|\cos(\iota)|$ , as this maps the occasional bimodal structure into a single PDF, and observing a compact merger at  $\iota$  and  $\iota + \pi/2$  should yield identical physics.

### 3.3. Sky Localization

Unlike the mass parameters, the recovery of the position on the sky is highly dependent on the location of the source with respect to the detector network in question. Much of the information about the sky position of the source comes from the relative timing of the signals in each detector. For the HLV configuration, timing in the three-detector network can only localize signals to one of two points in the sky. That is, when using only time-of-arrival information, there is equal support in the probability density functions near true location and near the point reflected through the plane formed by the three detectors. See Fairhurst (2011) for a global analysis of time-of-arrival accuracy for various network configurations, including those considered here.

In practice, however, additional information from the wave polarization and the relative difference in SNR between individual detectors can break this plane-reflection degeneracy, leading to a bi-modal distribution with significantly more support in one mode of the PDF. By fitting for the sky location and the polarization simultaneously, the MCMC can often identify the correct mode on the sky. For the four-detector configuration, this concern is irrelevant: even with time-of-arrival data alone, the HLVI network can constrain any source to a single mode on the sky. Even then, there are still locations on the sky in which two or more detectors are not sensitive to the gravitational-wave signal, yielding distorted, non-Gaussian PDFs.

The sky location uncertainties for HLV and HLVI are shown in Figures 6 and 7 respectively. We show all four mass bins together, since in practice the mass of the signals has little effect on the recovery of the sky location for the considered BNS systems. Only the location on the sky, the network configuration, and the other extrinsic parameters were found to be relevant. In particular, notice the increase in efficiency between the HLV configuration and the HLVI configuration. In the HLV configuration, there exist points on the sky in which the signal was injected near the plane of the detector network.

This causes the elongated, “banana-shaped” PDFs seen in Figure 6. In the HLVI configuration, the plane is no longer relevant, and there are substantially fewer regions in which only two detectors see a sufficiently strong signal. See Veitch et al. (2012) for a more detailed comparison of the sky-localization benefits of the HLVI configuration versus the three-detector network. For the HLV configuration, we find that all of the signals are recovered with a solid angle uncertainty of less than  $64 \text{ deg}^2$  ( $136 \text{ deg}^2$ ) at the 68% (95%) credible interval, while the HLVI configuration recovers all signals to less than  $14 \text{ deg}^2$  ( $45 \text{ deg}^2$ ). The median quantitative results for the two network configurations show a similar benefit with the addition of LIGO India, and are again reported in Table 2.

Two previous studies have considered the increase in sensitivity from the addition of the LIGO India site. Veitch et al. (2012) and Nissanke et al. (2013) studied the decrease in sky-location uncertainties obtained by the inclusion of the LIGO India site into the advanced detector network. Both studies employed an MCMC sampling technique (Veitch et al. via `LALInference`, Nissanke et al. via a modified version of `CosmoMC`), to determine the average parameter estimation uncertainties for a realistic distribution of sources in co-moving volume. As the current study is interested in the uncertainties of optimal sources at  $\text{SNR}_{\text{network}} = 20$ , ignoring the effects of less viable detection candidates, it is instructive to compare the 95% credible intervals between the three studies. The cumulative distributions of sky-area uncertainties for both network configurations in each study are plotted in Fig. 8.

### 3.4. Varied Noise Realizations

We have performed the current analysis on zero-noise injections for two reasons. First, the results of a zero-noise analysis are similar to those that would be achieved by averaging the results of multiple identical injections in different Gaussian noise realizations, as was argued in Section 2.3. The second reason is we are not able to predict the characteristics of realistic (often non-Gaussian) advanced detector noise. Attempting to do so would have little chance of being accurate while requiring a huge computational burden to combine the results of many MCMC runs in many different noise realizations.

In the case of a unique Gaussian realization of the Advanced LIGO noise curve, each realization causes the maximum likelihood of the posterior probability distribution to be translated away from the true value. These displacements tend to cancel over many runs, ensuring that the mean uncertainties should be nearly identical to the uncertainty drawn from the zero-noise runs. Again, this only holds in the case where a signal is sufficiently loud that the posterior is linear in the parameters  $\theta$ .

As a demonstration of this, we injected a single  $1M_{\odot}/2.5M_{\odot}$  system, detected in HLVI, into 5 separate realizations of Gaussian noise colored by the Advanced LIGO PSD, and compared the results to the same MCMC recovery in the zero-noise case. This example can be seen for one-dimensional marginalizations of  $M_c$  and  $q$  in Fig. 9. In effect, the “real answer” that will be recovered is a single PDF with similar width to the zero-noise PDF, but with the peak likelihood displaced from

the true value.

Of course, the largest concern for gravitational-wave parameter estimation will not be the specific realization of Gaussian noise, but the effects of non-Gaussianities in the data. Techniques which build off of the theoretical progress made in Allen et al. (2003); Rover (2011); Littenberg & Cornish (2010) for including glitches in our model for the data, and therefore relaxing the assumptions about stationary and Gaussian noise, are currently under investigation.

## 4. CREDIBLE INTERVALS

When quoting parameter estimation results, it is often convenient to reduce the full parameter space to credible intervals about single marginalized parameters.. To that end, we state the averaged 68% and 95% credible intervals about the single parameters for each of the three parameter pairs of interest. These were already plotted for the sky locations in Figures 6 and 7.

There are several different ways of computing the width of a credible interval in this setup. If one considers the points in the MCMC as random draws from the true posterior, then the  $\alpha$ -level credible interval can be computed by simply ordering the points, removing  $N(1 - \alpha)/2$  points from both sides of the posterior samples symmetrically, and measuring the width of the remaining points. While this procedure can prove hazardous for multi-modal distributions, it is straightforward and reliable for single-peaked distributions as reported here.

In Table 1, we list the mean 68% and 95% credible intervals recovered for the four mass configurations in both network configurations. This essentially quantifies the widths of the posteriors plotted throughout Section 3. The purpose of Tables 1 and 2 is to provide a quantitative and quotable source for studies seeking to determine how well a physical question about BNS systems can be answered with the Advanced LIGO/Virgo network.

Given the previous reliance of parameter estimation studies on the Fisher Information Matrix, it is informative to compare the credible intervals quoted here to previously reported values in the literature. We recompute the credible intervals of the chirp mass and the symmetric mass ratio ( $\eta \equiv m_1 m_2 / M_{\text{tot}}^2$ ) at the 68% level ( $1-\sigma$ ) for the  $1.4M_{\odot}/1.4M_{\odot}$  system presented here. We then compare the findings of the MCMC to the Fisher matrix predictions using an identical network configuration (HLV), noise curve, and waveform model. We compute the Fisher matrix uncertainties using a code previously described in Rodriguez et al. (2013). We find that the MCMC credible intervals vary significantly from the estimates of the Fisher matrix, with the Fisher matrix underestimating the fractional uncertainties by as much as a factor of three. See Table 3. This disagreement, while unsurprising, emphasizes the importance of employing the full parameter estimation machinery of an MCMC when making physically relevant claims.

## 5. CONCLUSION

In this paper, we performed an MCMC parameter estimation analysis on the recoverability of basic information about binary neutron stars, using two projected versions of the Advanced LIGO/Virgo network. We focused on the recovery of the two masses, the luminosity distance,

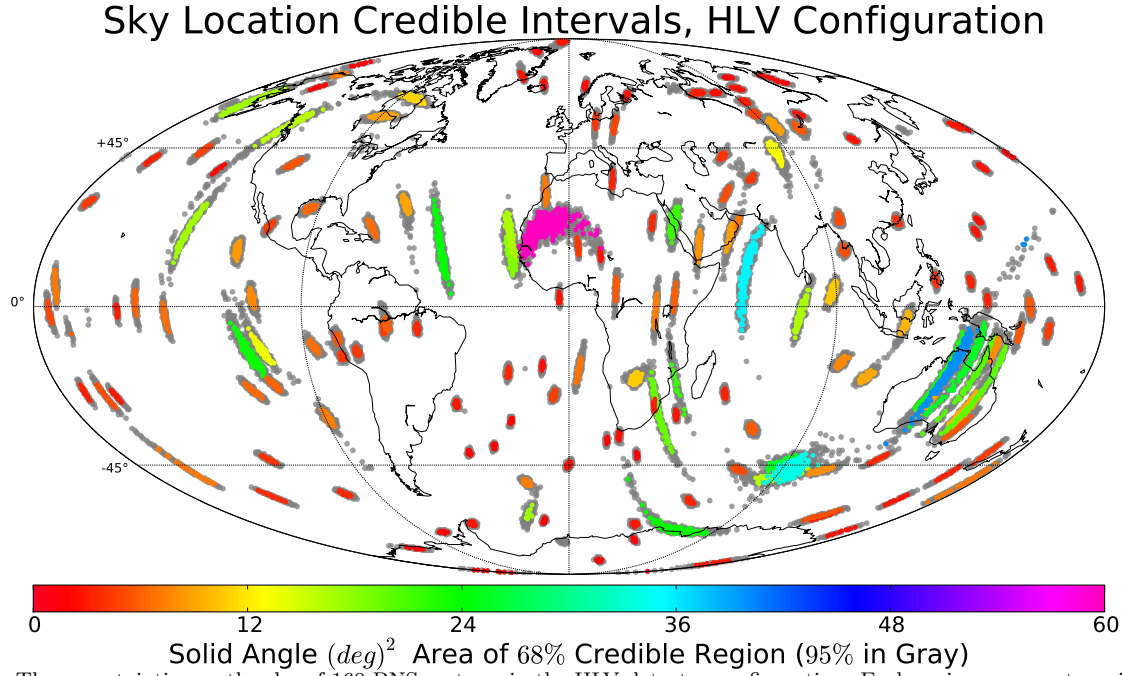


FIG. 6.— The uncertainties on the sky of 160 BNS systems in the HLV detector configuration. Each region represents a single injection, with the colored central region representing the 68% uncertainty region on the sphere, and the gray shade representing the 95% uncertainty region. The color scheme indicates the total solid angle size of the 68% region. Note the similar shape of the uncertainty regions at particular points; this is due to the specific pattern of sensitivity over the sky for the three-detector network.

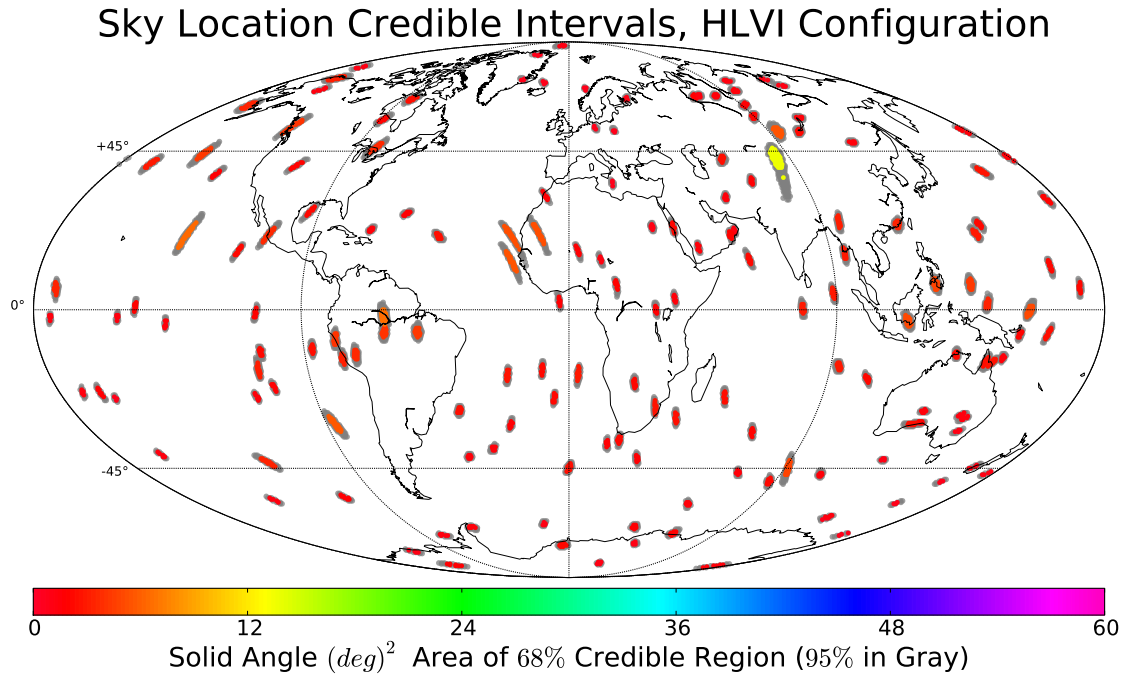


FIG. 7.— The same as Fig 6, except for the HLVI detector configuration. Note the substantially lower average uncertainties on the skies for the majority of the injections. Also note the lack of large, “banana-shaped” uncertainties that were recovered by the HLV configuration. The two improvements are due to the breaking of the plane degeneracy that is facilitated by the transition to a four-detector network.

orbital inclination, and the sky location, as these are the six basic parameters of physical interest to the problem. We found that, neglecting the effects of spin, the component masses can be constrained to within 9% (15%) of

their true value to a credible level of 68% (95%). This value drops below 1.9% (3.7%) for systems with an asymmetric mass ratio. These results were summarized in Table 1. It should be remembered that these signals were

TABLE 1

MEDIAN 68% AND 95% CREDIBLE INTERVALS FOR INTRINSIC PARAMETERS FOR EACH OF THE FOUR SYSTEMS CONSIDERED. WE REPORT THE CREDIBLE INTERVALS OF QUANTITIES MEASURED, AS WELL AS THE COMPONENT MASSES AND TOTAL MASS. ALTHOUGH THE RESULTS FOR THE HLV AND HLVI CONFIGURATIONS ARE QUANTITATIVELY IDENTICAL, WE REPORT THEM SEPARATELY FOR CONSISTENCY.

HLV

System	$\Delta\mathcal{M}_c/\mathcal{M}_c$		$\Delta M_1/M_1$		$\Delta M_2/M_2$		$\Delta M_{tot}/M_{tot}$		$\Delta q$	
Credible Level	68%	95%	68%	95%	68%	95%	68%	95%	68%	95%
$1M_\odot - 1M_\odot$	0.00497%	0.0104%	7.17%	11.9%	6.39%	10.3%	0.643%	1.25%	0.123	0.197
$1.4M_\odot - 1.4M_\odot$	0.00883%	0.0188%	7.77%	13%	6.87%	11.1%	0.746%	1.47%	0.132	0.212
$1M_\odot - 2.5M_\odot$	0.0176%	0.0355%	1.86%	3.74%	1.59%	3.23%	1.48%	2.99%	0.0138	0.028
$2.5M_\odot - 2.5M_\odot$	0.0246%	0.0522%	9.02%	15%	7.82%	12.6%	1.01%	1.94%	0.149	0.239

HLVI

System	$\Delta\mathcal{M}_c/\mathcal{M}_c$		$\Delta M_1/M_1$		$\Delta M_2/M_2$		$\Delta M_{tot}/M_{tot}$		$\Delta q$	
Credible Level	68%	95%	68%	95%	68%	95%	68%	95%	68%	95%
$1M_\odot - 1M_\odot$	0.00497%	0.0106%	7.15%	11.9%	6.38%	10.4%	0.646%	1.27%	0.123	0.198
$1.4M_\odot - 1.4M_\odot$	0.00884%	0.0188%	7.67%	12.8%	6.79%	11.1%	0.733%	1.46%	0.13	0.211
$1M_\odot - 2.5M_\odot$	0.0176%	0.0352%	1.85%	3.72%	1.59%	3.2%	1.47%	2.96%	0.0137	0.0277
$2.5M_\odot - 2.5M_\odot$	0.0243%	0.0515%	9.03%	14.9%	7.84%	12.6%	0.998%	1.92%	0.149	0.238

TABLE 2

MEDIAN 68% AND 95% CREDIBLE INTERVALS OF EXTRINSIC PARAMETERS FOR EACH OF THE FOUR SYSTEMS CONSIDERED. AS EXPECTED, THERE EXISTS A SUBSTANTIAL IMPROVEMENT IN THE SKY LOCALIZATION CAPABILITIES OF THE FOUR-DETECTOR HLVI CONFIGURATION OVER THE THREE-DETECTOR HLV CONFIGURATION. NOTE THAT THE SOLID-ANGLE SKY-LOCATION CREDIBLE INTERVALS,  $\Delta\Omega$ , ARE CALCULATED DIRECTLY ON THE 2D SPHERE, NOT BY COMBINING THE  $\alpha$  AND  $\delta$  UNCERTAINTIES.

HLV

System	$\Delta D$ (mpc)		$\Delta  \cos(\iota) $		$\Delta\alpha$ (deg)		$\Delta\delta$ (deg)		$\Delta\Omega$ (deg $^2$ )	
Credible Level	68%	95%	68%	95%	68%	95%	68%	95%	68%	95%
$1M_\odot - 1M_\odot$	49.4	89.9	0.323	0.611	1.73	4.09	2.51	5.52	5.12	13.5
$1.4M_\odot - 1.4M_\odot$	61.4	107	0.314	0.588	2.63	5.42	2.53	5.27	4.12	11.2
$1M_\odot - 2.5M_\odot$	68.8	127	0.31	0.549	2.41	4.6	2.77	6.2	4.37	12.1
$2.5M_\odot - 2.5M_\odot$	116	198	0.349	0.613	1.75	4.51	2.42	5.01	4.62	12

HLVI

System	$\Delta D$ (mpc)		$\Delta  \cos(\iota) $		$\Delta\alpha$ (deg)		$\Delta\delta$ (deg)		$\Delta\Omega$ (deg $^2$ )	
Credible Level	68%	95%	68%	95%	68%	95%	68%	95%	68%	95%
$1M_\odot - 1M_\odot$	42.7	76.2	0.267	0.455	1.13	2.25	1.48	3.01	1.87	5.37
$1.4M_\odot - 1.4M_\odot$	66.6	121	0.285	0.509	1.27	2.48	1.49	3.01	2	5.12
$1M_\odot - 2.5M_\odot$	73.7	130	0.297	0.499	1.29	2.42	1.42	2.89	1.75	4.87
$2.5M_\odot - 2.5M_\odot$	120	213	0.301	0.517	1.18	2.34	1.55	3.14	2.25	5.99

injected at high, but not unrealistic, SNRs. Thus, the results quoted can be thought of as the average uncertainties for a “good” Advanced LIGO/Virgo detection.

We also reported on the ability of the two network

configurations to constrain the luminosity distance and orbital inclination. For distance, it was found that the uncertainties will average anywhere from 43 to 120 MPC at 68% credible levels, and from 76 to 213 MPC at 96% credible levels, making the uncertainties larger than the luminosity distances themselves in many cases. Furthermore, it was found that the cosine of the orbital inclination can be constrained to within 0.35 (0.61) at the 68% (95%) level on average, suggesting that Advanced LIGO/Virgo will not be able to offer constraining information on GRB beaming angles in coincidence with electromagnetic observations. Coincidence detections will still be possible, but the orbital orientation information from gravitational waves will not provide astrophysically relevant constraints.

Finally, we reported the ability of advanced networks

TABLE 3  
68% CREDIBLE INTERVALS VERSUS 1- $\sigma$  FISHER MATRIX  
UNCERTAINTIES FOR MASS PARAMETERS IN EACH SYSTEM IN THE  
HLV CONFIGURATION.

Parameter	$\Delta\mathcal{M}_c/\mathcal{M}_c$		$\Delta\eta/\eta$	
Estimate	MCMC	FIM	MCMC	FIM
$1M_\odot - 1M_\odot$	0.00497%	0.00205%	0.645%	0.321%
$1.4M_\odot - 1.4M_\odot$	0.00890%	0.00384%	0.745%	0.380%
$1M_\odot - 2.5M_\odot$	0.0176%	0.00457%	1.475%	0.400%
$2.5M_\odot - 2.5M_\odot$	0.0245%	0.0114%	1.000%	0.612%

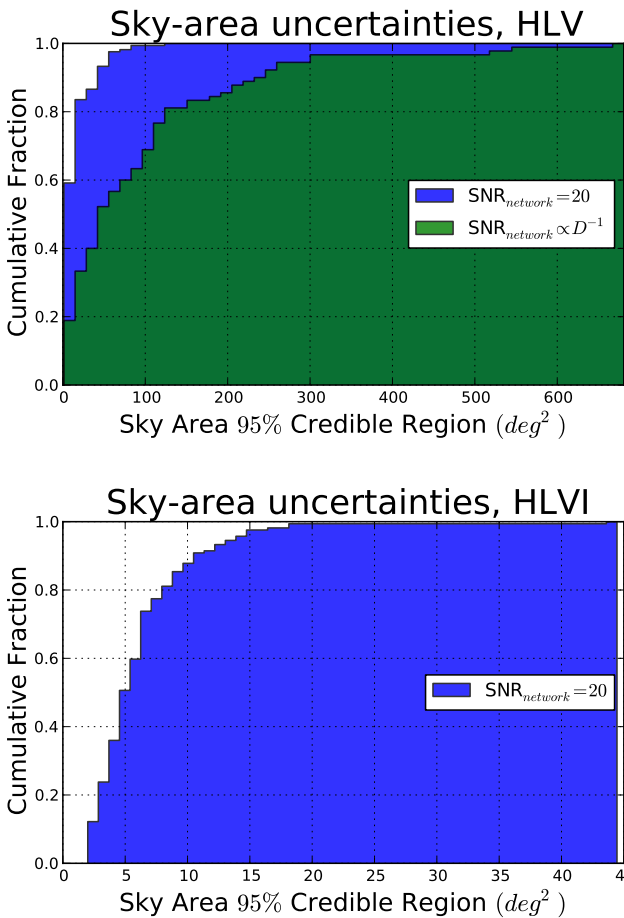


FIG. 8.— The cumulative fraction of sources found within  $\text{deg}^2$  at the 95% credible interval. This plot contains results from three separate studies: the current study, in which optimal detection candidates are considered ( $\text{SNR}_{\text{network}} = 20$ ), Veitch et al. (2012), which employs several LALInference samplers (including the MCMC sampler used here) on an source population evenly distributed in co-moving volume, and Nissanke et al. (2013), which employs a separate MCMC code on a realistic source population. The optimal detection candidates are constrained to substantially smaller solid angles on the sky, as is expected for such “gold-plated” events.

to constrain the sky location of BNS signals. It was found that the three-detector configuration, consisting of the Washington and Louisiana LIGO sites plus the Italian Virgo site, was able to constrain all signals within  $64 \text{ deg}^2$  ( $136 \text{ deg}^2$ ) on the sky at the 68% (95%) credible level, with an average median 68% (95%) credible interval of  $4.6 \text{ deg}^2$  ( $12.2 \text{ deg}^2$ ). Meanwhile, the four-detector configuration, consisting of the three-detector sites plus a LIGO India detector, was able to localize all the sky locations to within  $14 \text{ deg}^2$  ( $45 \text{ deg}^2$ ) on the sky at the 68% (95%) credible interval, with an average median 68% (95%) credible interval of  $2 \text{ deg}^2$  ( $5.3 \text{ deg}^2$ ).

It should be noted that there are two distinct types of systematic error, highly relevant to the gravitational-wave parameter estimation problem, that we have not addressed in this study. First, we have studied the parameter estimation uncertainties under the assumption

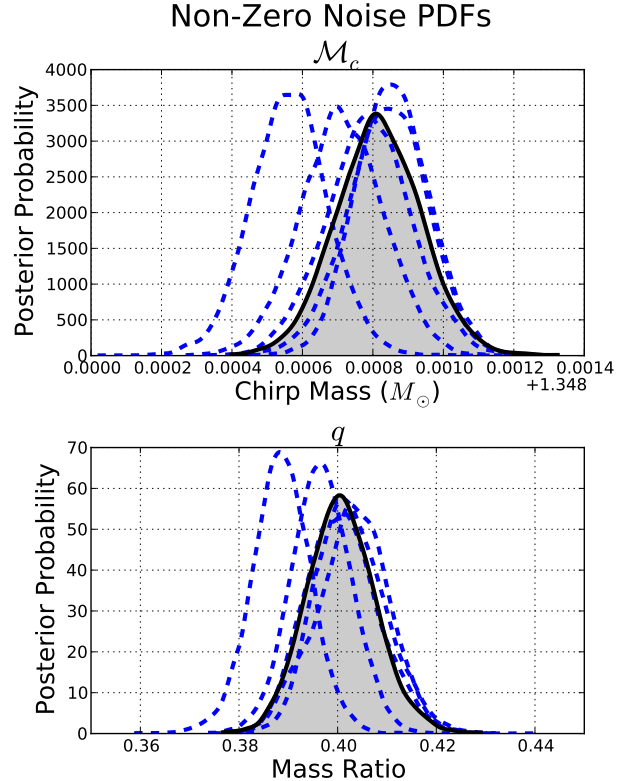


FIG. 9.— The effects of a non-zero noise realization on the recovered PDF for five different Gaussian realizations of the Advanced LIGO noise curve. Each blue-dashed PDF represents the recovery of the same  $1M_{\odot}/2.5M_{\odot}$  signal in a different noise curve, picked at random from the Gaussian colored noise defined by the Advanced LIGO power spectral density, while the gray-shaded curve is the zero-noise PDF. Notice how each curve is a Gaussian PDF with roughly similar shape, but different mean, to the zero-noise PDF. This only holds true for glitch-free data, which is an unrealistic idealization when compared to real data.

that the waveform template we use to recover the signal template exactly matches the fully relativistic waveforms nature provides. In practice, these waveforms are only approximations to the fully general-relativistic physics required to solve the problem. See Buonanno et al. (2009) for a better description of the systematic uncertainties present in the most common waveform families. Additionally, there are several astrophysical assumptions that can potentially contribute to systematic uncertainties in the waveforms, such as the neutron-star equation of state, possible modifications to General Relativity, eccentricity, etc.

Secondly, as stated above, we have performed our study under idealized detector-noise conditions. In practice the noise levels of Advanced LIGO and Advanced Virgo can vary with time and contain occasional excursions which are highly non-Gaussian. Unfortunately, there is no reliable way to predict the sort of non-Gaussian detector glitches and instrumentation effects that will arise in any advanced gravitational-wave detector. The realization of noise will be a major factor in the deflection of signal PDFs from the idealized cases presented here.

In this study, we have also neglected the effects of spin in the parameter space, electing to focus on the abso-

lute basic parameters that will be measured routinely in the Advanced Detector era. Given the high degree of coupling between the spin and mass of objects in the gravitational-wave parameter space, it remains unclear if the mass measurement alone will be sufficient to dis-

tinguish non-spinning neutron stars from highly-spinning low-mass black holes. Future work will explore this potential mass/spin degeneracy, including the effects of orbital precession, with the aim of definitively answering this question.

## REFERENCES

- Abadie, J., Abbott, B. P., Abbott, R., et al. 2010, *The Astrophysical Journal*, 715, 14531461, 14531461
- Abadie, J., Abbott, B. P., Abbott, R., et al. 2010, *Classical and Quantum Gravity*, 27, 173001, 173001
- Abadie, J., Abbott, B. P., Abbott, R., et al. 2012, *Physical Review D*, 85, 082002, 082002
- Allen, B., Creighton, J. D., Flanagan, E. E., & Romano, J. D. 2003, *Phys. Rev. D*, 67, 122002, 122002
- Arun, K. G., Iyer, B. R., Sathyaprakash, B. S., & Sundararajan, P. A. 2005, *Phys. Rev. D*, 71, 084008, 084008
- Baird, E., Fairhurst, S., Hannam, M., & Murphy, P. 2013, *Phys. Rev. D*, 87, 024035, 024035
- Buonanno, A., Iyer, B. R., Ochsner, E., Pan, Y., & Sathyaprakash, B. S. 2009, *Phys. Rev. D*, 80, 084043, 084043
- Corsi, A., Collaboration, f. t. L. S., & Collaboration, f. t. V. 2012, 8, 8
- Cutler, C., & Flanagan, É. E. 1994, *Phys. Rev. D*, 49, 2658, 2658
- Fairhurst, S. 2011, *Classical and Quantum Gravity*, 28, 105021, 105021
- Finn, L. S. 1992, *Phys. Rev. D*, 46, 5236, 5236
- Gilks, W. R. 1999, *Markov Chain Monte Carlo In Practice*
- Hannam, M., Brown, D. A., Fairhurst, S., Fryer, C. L., & Harry, I. W. 2013, *Astrophys. J. Lett.*, 766, L14, L14
- Harry, G. M., & the LIGO Scientific Collaboration. 2010, *Classical Quant. Grav.*, 27, 084006, 084006
- Hinderer, T., Lackey, B. D., Lang, R. N., & Read, J. S. 2010, *Physical Review D*, 81, 123016, 123016
- Kalogera, V., Kim, C., Lorimer, D. R., et al. 2004, *Astrophys. J. Lett.*, 601, L179, L179
- Kim, C., Kalogera, V., & Lorimer, D. R. 2006, ArXiv Astrophysics e-prints, arXiv:astro-ph/0608280
- Li, T. G. F., Del Pozzo, W., Vitale, S., et al. 2012, *Physical Review D*, 85, 082003, 082003
- Littenberg, T. B., & Cornish, N. J. 2010, *Phys. Rev. D*, 82, 103007, 103007
- Metzger, B. D., & Berger, E. 2012, *Astrophys. J.*, 746, 48, 48
- Nakar, E. 2007, *Physics Reports*, 442, 166236, 166236
- Nissanke, S., Holz, D. E., Hughes, S. A., Dalal, N., & Sievers, J. L. 2010, *Astrophys. J.*, 725, 496, 496
- Nissanke, S., Kasliwal, M., & Georgieva, A. 2013, *Astrophys. J.*, 767, 124, 124
- Nissanke, S., Sievers, J., Dalal, N., & Holz, D. 2011, *Astrophys. J.*, 739, 99, 99
- O'Shaughnessy, R., Kalogera, V., & Belczynski, K. 2010, *Astrophys. J.*, 716, 615, 615
- Oslowski, S., Bulik, T., Gondek-Rosińska, D., & Belczyński, K. 2011, *Mon. Not. R. Astron. Soc.*, 413, 461, 461
- Poisson, E., & Will, C. M. 1995, *Phys. Rev. D*, 52, 848, 848
- Raymond, V., van der Sluys, M. V., Mandel, I., et al. 2010, *Classical and Quantum Gravity*, 27, 114009, 114009
- Rodriguez, C. L., Farr, B., Farr, W., & Mandel, I. 2013, arXiv:Working on it...
- Rover, C. 2011, *Phys. Rev. D*, 84, 122004, 122004
- Shoemaker, D. 2009, *Advanced LIGO anticipated sensitivity curves*
- the LIGO Scientific Collaboration, the Virgo Collaboration, Aasi, J., et al. 2013, ArXiv e-prints, arXiv:1304.1775
- Vallisneri, M. 2008, *Phys. Rev. D*, 77, 042001, 042001
- van der Sluys, M., Mandel, I., Raymond, V., et al. 2009, *Classical and Quantum Gravity*, 26, 204010, 204010
- Veitch, J., & Vecchio, A. 2010, *Phys. Rev. D*, 81, 062003, 062003
- Veitch, J., Mandel, I., Aylott, B., et al. 2012, *Phys. Rev. D*, 85, 104045, 104045
- Virgo Collaboration. 2009, *Advanced Virgo Baseline Design*,